Synthesis of Densely Packaged, Ultrasmall Pt02Clusters within a Thioether-Functionalized MOF: Catalytic Activity in Industrial Reactions at Low Temperature

Synthesis of densely-packaged, ultrasmall Pt^0_2 clusters within a thioether functionalised MOF and their catalytic activity in industrial reactions at low–temperature

Marta Mon,[a] Miguel A. Rivero–Crespo,[b] Jesús Ferrando–Soria,[a] Alejandro Vidal–Moya,[b] Mercedes Boronat,[b] Antonio Leyva–Pérez,*[b] Avelino Corma,*[b] Juan C. Hernández–Garrido,[c,d] Miguel López–Haro,[c,d] José J. Calvino,[c,d] Giulio Ragazzon,[e] Alberto Credi,[e,f] Donatella Armentano*[g] and Emilio Pardo*[a]

Abstract: The gram-scale synthesis, stabilization and characterization of well-defined ultrasmall subnanometric catalytic clusters on solids represent a challenge. Here, we report the chemical synthesis and X-ray snapshots of Pt_2^0 clusters, homogenously distributed and densely-packaged within the channels of a metal-organic framework. This novel hybrid material catalyzes efficiently, and even most important from an economic and environmental viewpoint, at low temperature (25 to 140 ºC), energetically–costly industrial reactions in the gas phase such as hydrogen cyanide (HCN) production, carbon dioxide (CO_2) methanation and alkene hydrogenations. These results open the way for the design of precisely–defined catalytically active ultrasmall metal clusters in solids for technically easier, cheaper and dramatically–less dangerous industrial reactions.

Sub–nanometer metal clusters (sMCs),[1–5] consisting of small aggregations of atoms exposed to the external environment, have emerged as excellent catalysts for organic reactions of industrial interest.[6,7] Unfortunately, their synthesis and stabilization is still a challenge.[8] Supporting sMCs on the appropriate porous matrix[5] has been proven as an efficient strategy to overcome the mentioned problems. Nevertheless, much efforts are still needed to exactly control atomicity, electronics, structure and metal loading of the sMCs.

Metal–Organic Frameworks (MOFs),[9–11] a type of crystalline porous materials, are, potentially, good platforms to synthesize sMCs in a controlled manner. In this context, information about their nature might be gained by single crystal X–ray crystallography (SC–XRC),[12,13] in combination with more common characterization techniques for solid supported metals such as X–ray photoelectron spectroscopy (XPS), Fourier transform infrared spectroscopy under CO (FTIR–CO) or aberration–corrected scanning transmission electron microscopy (AC–STEM).[12,14] Despite some examples of MOFs hosting small metal nanoclusters of 1–3 nm,[15–19] it is difficult to find MOFs with metal species below the nanometer.[12] A successful development of this type of materials, also considering the well–known ability of MOFs to adsorb gas molecules,[11] could lead to a more efficient, economic and safe way to carry out a variety of reactions of technological interest[20] requiring the activation of gases.

Herein, we report the chemical synthesis, and structural and electronic well–defined characterization, of Pt^0_2 clusters within the functional channels of a MOF, decorated with thioether recognition sites, intrinsically devoted for this purpose. This new synthetic route to sMCs represent a step-forward respect a previously described method,[12] whose applicability is limited to anionic MOFs. The obtained Pt^0_2–MOF material catalyzes reactions, very important from an industrial point of view, such as the room temperature NH_4CN production[21], after concomitant activation of CO and NH_3, the methanation of CO_2[22–24] and the hydrogenation of ethylene and ≤C6 olefins at <140 ºC, showing the high intrinsic catalytic activity of the Pt^0_2 sMCs for a variety of industrial reactions in the gas phase[25]

Figure 1 shows the synthesis of the Pt^0_2–MOF material in 3 steps. First, a robust and water–stable 3D MOF, prepared with a ligand derived from the amino acid *L*-methionine, of formula $\{Ca^{II}Cu^{II}_6[(S,S)\text{–methox}]_3(OH)_2(H_2O)\} \cdot 16H_2O$ (**1**)[26,27] (Figure 1a), featuring pores decorated with thio–alkyl chains, was prepared as the starting material. Then, Pt^{2+} cations were incorporated by anchoring the metal salt $K_2[PtCl_4]$ to **1** through the S atoms of the coordination network, yielding $(Pt^{II}Cl_2)_2@\{Ca^{II}Cu^{II}_6[(S,S)\text{–methox}]_3(OH)_2(H_2O)\} \cdot 13H_2O$ (**2**) (Figure 1b). Finally, the Pt_2 units were obtained by reduction of **2** with $NaBH_4$, to give $(Pt^0_2)_{0.5}(Pt^{II}Cl_2)@\{Ca^{II}Cu^{II}_6[(S,S)\text{–methox}]_3(OH)_2(H_2O)\} \cdot 15H_2O$ (**3**) (Figure 1c). Interestingly, **2** and **3** show a high loading of platinum atoms (ca. 17 wt% for both **2** and **3**), 50% of which are Pt^0_2 clusters in **3**. The nature of the Pt^0_2 units in **3** was established by combining SC–XRC using synchrotron radiation (Figures 1 and S1–S8) and AC–STEM (Figures 2 and S9–S14),

[a] M. Mon, Dr. J. Ferrando-Soria, Dr. E. Pardo
Instituto de Ciencia Molecular (ICMOL). Universitat de València
Paterna 46980, València (Spain)
E-mail: emilio.pardo@uv.es
[b] M. A. Rivero–Crespo, A. Vidal–Moya, Dr. M. Boronat, Dr. A. Leyva–Pérez, Prof. Dr. A. Corma
Instituto de Tecnología Química (UPV–CSIC). Universidad Politècnica de Valencia–Consejo Superior de Investigaciones Científicas. Avda. de los Naranjos s/n, 46022 Valencia, Spain
E-mail: anleyva@itq.upv.es, acorma@itq.upv.es
[c] Dr. J. C. Hernández–Garrido, Dr. M. López–Haro, Prof. J. J. Calvino
Departamento de Ciencia de los Materiales e Ingeniería Metalúrgica y Química Inorgánica. Facultad de Ciencias. Universidad de Cádiz, Campus Río San Pedro, 11510 Puerto Real, Cádiz, Spain
[d] Dr. J. C. Hernández–Garrido, Dr. M. López–Haro, Prof. J. J. Calvino
Instituto Universitario de Investigación en Microscopía Electrónica y Materiales (IMEYMAT). Facultad de Ciencias. Universidad de Cádiz, Campus Río San Pedro, 11510 Puerto Real, Cádiz, Spain
[e] G. Ragazzon, Prof. Dr. Alberto Credi
Dipartimento di Chimica "G. Ciamician", University of Bologna.
Via Selmi 2, 40126 Bologna, Italy
[f] Prof. Dr. Alberto Credi
Dipartimento di Scienze e Tecnologie Agro–alimentari, University of Bologna, Viale Fanin 50, 40127 Bologna, Italy
[g] Dr. D. Armentano
Dipartimento di Chimica e Tecnologie Chimiche
Università della Calabria. 87030, Rende, Cosenza, Italy
E-mail: donatella.armentano@unical.it

Supporting information for this article is given via a link at the end of the document.

which allowed unprecedented snapshots of such tiny clusters at the atomic level. Inductively coupled plasm–mass spectrometry (ICP–MS), elemental analysis, powder X–ray diffraction (PXRD) and thermo–gravimetric (TGA) analyses (see Supporting Information, Figures S15, S16 top and Table S1), in combination with XPS, FTIR–CO spectroscopy (Figures S17 and S18) and DFT calculations (Figure S19), were also used to establish the structure and oxidation state of Pt.

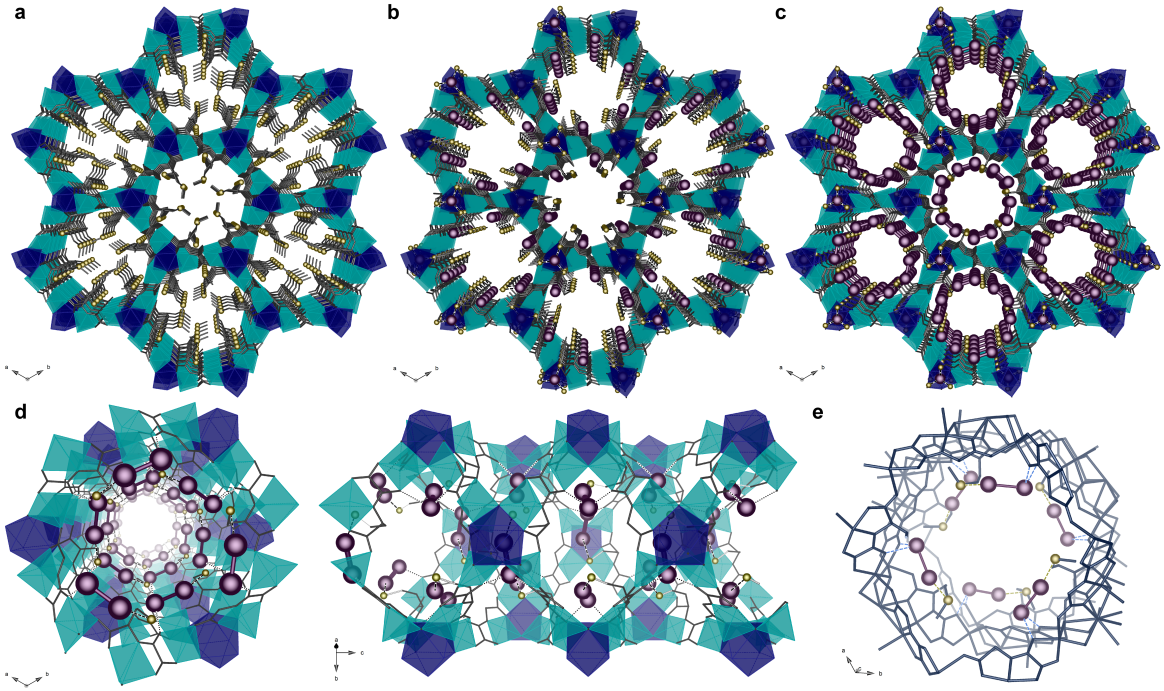

Figure 1. Crystal structures of the MOFs **1** (**a**) **2** (**b**) and **3** (**c**). **d**, determined by single-crystal X-ray diffraction. Perspective views, in detail, of a channel of **3** in the *ab* (left) and *bc* (right) planes. Copper and calcium atoms from the network are represented by cyan and blue polyhedra, respectively, whereas organic ligands are depicted as grey sticks. Yellow and purple spheres represent S and Pt atoms, respectively. Dashed lines represent the Pt···S interactions. **e**. Fragment of a channel of **3** emphasizing the interactions with the network. Pt–S and Pt···O interactions are represented by yellow and blue dashed lines, respectively.

The crystal structures of **2** and **3** are isomorphous and crystallize in the chiral $P6_3$ space group, like the ancestor **1**, exhibiting a common chiral honeycomb–like 3D calcium(II)–copper(II) framework. These uni–nodal six–connected acs networks (point symbol $4^9{\cdot}6^6$) feature hexagonal channels, where the highly flexible thioalkyl chains (Figures S1–S5 and video S1), remain confined and adopt conformations depending on the nature of guests, Pt^{2+} in **2** (Figures 1a, S1 and S3) or both Pt^{2+} and Pt^0_2 NCs in **3** (Figures 1b, 1c, S2, S4 and S5). The values of the Pt^{2+}–S bond distances [2.46(5) and 2.34(3) Å (**2**) (Figure S1a) and 2.25(3)-2.41(3) Å (**3**), Figure S2b] are similar to typical values reported in the literature.[28,29] On the other hand, the Pt^0–S distance is 2.30(4) Å (**3**) (Figure S1b). Each Pt^{2+} ion is, as expected, further surrounded by chloride atoms [Pt-Cl = 2.52(4) Å in **2** and 2.42(4)/2.48(4) Å in **3**] (see crystallographic section in SI). The conformation of the MOF's thioalkyl arms evidences chain intrinsic flexibility, with one of the two asymmetric moieties exhibiting a distended conformation inward the pores, grasping a fraction of guest molecules, and forcing the other one in an extremely bent conformation of the methyl groups to pinpoint a 50% of total Pt^{2+} ions in poorly accessible interstitial sites, pointing along *c* axis (Figures S1a, S3–S5). The conformation observed in **2** (Figures S1a and S3) is also adopted in **3** (Figures S2b, S4–S5a**)** where, in turn, Pt^0_2 dimers with a Pt–Pt distance of 2.49(6) Å are unambiguously observed (Figures 1b,c and S1b–S5). As far as we know, no reports on crystallographically precise Pt^0_2 dimers appeared so far, the only experimental data recording on Pt^0–Pt^0 distance in sMCs indicates a value of 2.65 Å, extrapolated from X–ray absorption fine structure spectrum (EXAFS).[5] Pt^0_2 dimers weakly interact also with oxamate moieties with Pt···O distances of 2.79(1) and 2.80(1) Å (Figures 1d–e; see also Supporting Information Figures S4 and S5). Periodic DFT calculations support the crystallographic characterization of **3**, with optimized distances Pt^0–Pt^0 = 2.43 Å, Pt^0–S = 2.18 Å, Pt^{2+}–S = 2.32 – 2.34 Å and Pt^{2+}–Cl = 2.26 Å, and the proposed electronic distribution, with calculated atomic charges of -0.10 and -0.03 for Pt^0 and 0.46 – 0.49 e^- for Pt^{2+} (Figure S19).

Figure S6 shows a plausible mechanism for the formation of the Pt^0_2 dimers in **3**, driven by the flexibility of the thio–ether groups anchoring Pt^{2+} metals in **2**, which most–likely approach two neighboring Pt^{2+}–S units located inside the pores, to build the Pt^0_2 units after the reduction process. Meanwhile, the mononuclear Pt^{2+} complexes residing in hindered interstitial voids are not reduced (Figure S2). Interestingly, the virtual diameter of the channels increases from *ca*. 0.3 nm in the precursor material **1** to *ca.* 0.8 nm in **2** and **3** (Figures S7 and S8), and N_2 adsorption isotherms at 77 K (Figure S16 bottom)

confirm the increased permanent porosity of both **2** and **3** compared to the starting material **1**.[27] The Brunauer-Emmett-Teller (BET) surface areas calculated for **1**, **2** and **3** are 153, 487 and 453 m^2/g, respectively, with pore sizes of 0.22, 0.61 and 0.57 nm, following a similar trend to that observed in the crystal structures (see Supporting Information for details).

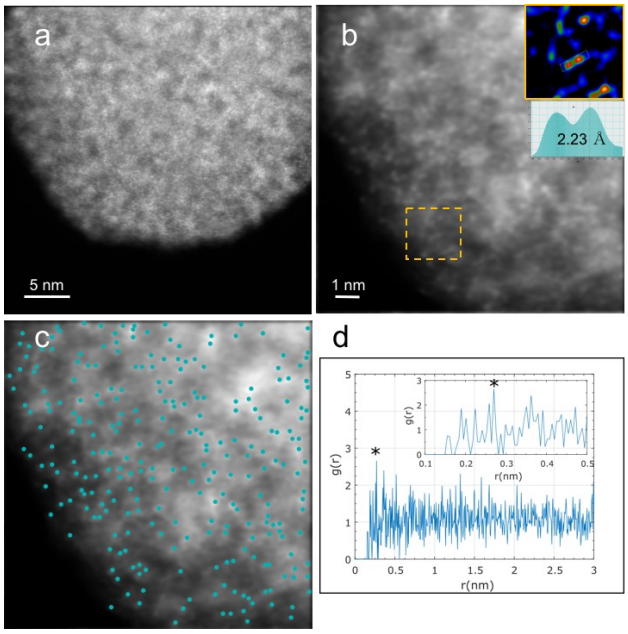

Figure 2. AC–HAADF–STEM analysis of **3**. The porous crystalline structure of the MOF is observed in (**a**). After denoising AC–HAADF–STEM image, the spatial distribution of the ultrasmall Pt clusters is clearly observed (**b**). Visualization is further improved after background subtraction and color displayed; inset in (**b**) corresponds to the dash–squared area. Lower inset in (**b**) illustrates an intensity profile on the Pt dimer marked in the upper inset. Overlay of the denoised AC–HAADF–STEM image and the *x*–*y* coordinates (green dots) obtained after template matching is shown in (**c**). The pair correlation function from the processed image is plotted in (**d**). A zoom of the small Pt–Pt distance range is shown as inset. The asterisk marks the position of the highest probability Pt–Pt distance at 0.283 nm.

Figures 2, S9 and S10 show AC–STEM images of **3** with high–angle annular dark field (HAADF) or Z–contrast imaging, coupled with chemical elemental maps by X–EDS in Figure S10. They allow a direct visualization of homogeneously distributed single Pt atoms (Pt^{2+} cations located in interstitial sites) and Pt_2 dimers (inset of Figure 2b and Figure S9) on the preserved crystalline framework, in accordance with SC–XRC measurements. The same Pt_2 dimers can be also inferred by HAADF-STEM images (Figure S11) of **3** after the hydrogenation of ethylene in flow for 4 hours on stream up to 60 ºC (Figure S11). The corresponding XEDS elemental mapping also shows a very homogenous distribution of Pt atoms after catalysis (Figure S12). Analysis of aberration corrected HR–TEM images (Figure S10a) allows to visualize the lattice fringes of the net, with interplanar spacing of 1.52 nm, which corresponds to (100) planes of the MOF and 0.30 nm (500) thus confirming that **3** retains crystallinity (Figure S10a). The combination of advanced image processing, based on combined Anscomb variance stabilization transform, wavelet–based filtering and background subtraction (Figures S13a–c), followed by template matching and pair correlation analysis tandem (Fig S13d–f), allowed detecting neighbors and next–nearest neighbors of each isolated atom on the Z–contrast images. This gives a pair correlation function *g*(r) (see Figures 2b–d, S13 and S14), which informs about the probability of finding the center of an atom at a given distance from the center of another atom (further details can be found in the Supporting Information). Applying this analysis to a large set of experimental images (two of them are shown in Figure S14), provided an average Pt–Pt distance of 0.262 nm. Indeed, this value is in very good agreement with single–crystal X–ray diffraction measurements.

Deconvoluted XPS of compound **2** (Figure S17a) shows a typical $Pt4f_{7/2}$ doublet for Pt^{2+} at 73.8 and 77.2 eV, while **3** (Figures S17b–c) shows two additional peaks at 72.1 and 75.6 eV, which correspond to Pt^0. The progressive increase of the latter at expenses of the former when using increasing amounts of reducing agent, up to 50%, is in good agreement to the expected reduction of the Pt^{2+} accessible atoms when treated with solvated BH_4^- in solution. Low–temperature FTIR–CO spectroscopy of **2** (Figure S18a) shows three signals at 2154, 2136 and 2104 cm^{-1}, which can be assigned to free CO, CO coordinated to Pt^{2+} atoms in the pores, and CO coordinated to the Pt^{2+} atoms in interstitial positions, respectively[30]. In contrast, **3** (Figure S18b) shows a dramatic decrease of the signal at 2136 cm^{-1} at expenses of the appearance of a new band at 1870 cm^{-1}, which can be assigned to CO coordinating two Pt^0 atoms.[31] These results strongly support that only one fraction of the Pt^{2+} atoms in **2**, probably the most accessible ones, is reduced with BH_4^-, while the inaccessible, interstitial Pt^{2+} atoms are unaltered during the process (see Figure S6).

UV–visible absorption spectra obtained from diffuse reflectance measurements (Figure S20) reveals that compound **3** exhibits a significantly higher absorbance between 300 and 400 nm, which supports the presence of the Pt^0 dimers,[32,33] together with the *d*–*d* transitions between 600 and 900 nm corresponding to Cu ions. PXRD patterns of **2** and **3** (Figure S15) confirm the pureness of the bulk samples (being isostructural to those crystals selected for SC–XRC), and that the open–framework structures remain unchanged after the insertion of the Pt salt in **2** (Figure S15a) and the reduction process to yield **3** (Figure S15b). No peaks of Pt NPs or oxide crystal structures in the PXRD pattern of **3** (Figure S15b) were found, which is consistent with the characterization results presented above, indicating that only Pt^0_2 sMCs are formed after the reduction process to yield **3**. Finally, PXRD patterns after the hydrogenation of ethylene in flow for 4 hours on stream up to 60 ºC (**3'** exp in Figure S15b), also showed no peaks indicative of agglomeration.

Figure 3a shows the results for the Pt–catalyzed reaction of NH_3 with CO at room temperature. Only **2** and **3** showed catalytic activity among 20 different Pt catalysts, including Pt salts, complexes and supported nanoparticles, with an initial turnover frequency (TOF_0) = 1260 h^{-1}. The total turnover number (TON) for **3** was 56, double than for **2**. Kinetic experiments (Figure S21) show that the **3**–catalyzed reaction starts fast, without any induction period, and the reaction rate rapidly decreases. In contrast, **2** presents a reaction induction period. If

one supposes that Pt_2^0 are the catalytically active species, as indicated by the experiments with catalyst **3**, the induction period observed with catalyst **2** would be due to the time required to reduce Pt^{2+} into Pt_2^0. For studying how the reaction occurs on the catalyst, in–situ ^{13}C and ^{15}N cross–polarization magic angle spinning nuclear magnetic resonance (CP/MAS–NMR) experiments with 0.5 and 1 ML of isotopically labelled ^{13}CO and $^{15}NH_3$, respectively, were adsorbed in **3** at room temperature and pressure. The results (Figure S22) show the progressive disappearance of ^{13}CO and $^{15}NH_3$, and the progressive appearance of two new peaks at 165 (^{13}C) and -255 (^{15}N) ppm, which can be assigned to adsorbed amide and oxime–type species.[34] These results agree well with the formation of an intermediate Pt amide species, which dehydrates directly to NH_4CN under the excess of NH_3 and circumvents HCN formation, as depicted in Figure 3a. Thus, it can be said that **3** has an extraordinary intrinsic catalytic activity for NH_4CN formation, which energetically by–passes (ΔH_{298}= -20 kcal mol^{-1}) the HCN formation (ΔH_{298}= +12 kcal mol^{-1})[35] (Figure S23). A NH_3 adsorption isotherm (Figure S24) shows that the MOFs **1** and **3** incorporate *ca.* 25 wt% of NH_3, which approaches the highest absorptivity values found in the literature for MOFs (20 wt%).[36] Temperature-programmed desorption of NH_3 in **1** and **3**, coupled to mass spectrometry (TPD-MS), shows that NH_3 desorbs unaltered at <120 ºC, after saturation of the samples at atmospheric pressure and room temperature (Figure S25). The ^{15}N CP/MAS–NMR of **3** after adsorbing isotopically labelled $^{15}NH_3$ (0.2 mmol x g^{-1}, 0.25 equivalents with respect to Pt) at low pressure and -196 ºC, further confirms the easy incorporation of NH_3 to the MOF structure (Figure S26).[37] Kinetic experiments at different partial pressures of CO (P_{CO}) and NH_3 (P_{NH3}), while maintaining a total pressure of 6 bars with N_2, show that the initial reaction rate only depends on P_{NH3} and not on P_{CO}, which supports that the Pt_2 sites are saturated with CO molecules and that the coupling with NH_3 on the Pt^0_2 catalytic sites, to form the amide intermediate, is the rate–determining step of the reaction. Analysis of the *post–mortem* solid catalyst (Figure S27) clearly shows the presence of two different cyanide species on the surface of **3**, which can be assigned to NH_4CN and Pt_2–CN species, respectively, which explain the decrease of activity of the catalyst during reaction. However, the results here open the way for the design of Pt^0_2 catalytic sites on more robust solids, which will result in intrinsically very active and long stable catalyst for HCN formation.

a

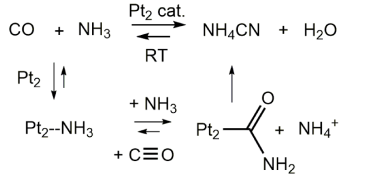

Entry	Catalyst	TON	TOF$_0$ (s^{-1})
1	–	–	–
2	$PtCl_4$	<1	–
3	$PtCl_2$	–	–
4	$Pt(acac)_2$	<1	–
5	PtO_2	–	–
6	$Na_2PtCl_6.xH_2O$	<1	–
7	$H_2PtCl_6.xH_2O$	–	–
8	$Pt(NH_3)_4(NO_3)_2$	–	–
9	$Pt(NH_3)_4(OH)_2$	–	–
10	$Pt(cod)Me_2$	–	–
11	$PtMe_3Cp$	–	–
12	$Pt(NH_3)_4Cl_2.xH_2O$	–	–
13	$Pt(PhCN)_2Cl_2$	–	–
14	$Pt(cod)Cl_2$	<1	–
15	Pt/C	–	–
16	Pt^{2+}/NaY	–	–
17	Pt/NaY	–	–
18	**1**	–	–
19	**2**	25	0.17
20	**3**	53	0.35

b

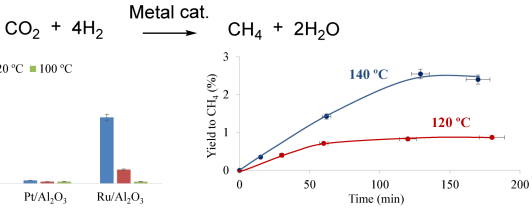

Catalyst[25]	Temperature (º C)	Reaction pressure (bar)	Activation energy (KJ mol^{-1})
Ni 58%	275–325	7–17	61
Ru/Al_2O_3 10wt%	200–300	1	66
Ru/Al_2O_3 0.5wt%	200–400	1	68
3	**100–140**	**4**	**35**

c

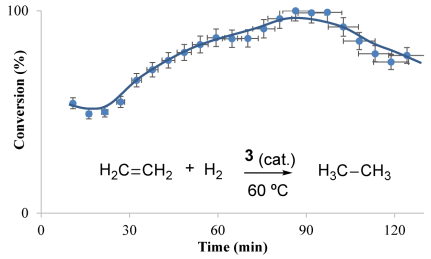

Catalyst	Temperature (º C)	Reaction pressure (bar)	Activation energy (KJ mol^{-1})
Pd/SiO_2	80–120	1	36
$Pd–Ag/SiO_2$	80–120	1	32
3	40–80	5	32

Figure 3. (**a**) Pt–catalysed synthesis of HCN at room temperature: Equation shows the reaction conditions: CO (4 bar, 1.5 mmol), NH_3 (2 bar, 0.75 mmol) and 0.0075 mmol Pt, and a plausible reaction mechanism. Table includes the set of Pt catalysts tested under these reaction conditions. (**b**) Pt–catalysed methanation of CO_2: Equation shows the reaction conditions: 7 ml CO_2 (1 atm, 0.28 mmol), 7 ml N_2 (internal standard, 1 atm, 0.28 mmol), 7 ml H_2 (4 atm, 1.12 mmol), MOF catalyst **2** and **3** (8 wt%, 20 mg, 0.008 mmol metal) or M/Al_2O_3 (5 wt%, 32 mg, 0.008 mmol metal), 100–140 ºC, 6 hours. Table includes reaction values for reference literature catalysts and catalyst **3**. (**c**) Pt–catalysed hydrogenation of ethylene: Equation shows the reaction conditions: 2 ml/min C_2H_4, 6 ml/min H_2, atmospheric pressure, 60 ºC, 50 mg **3** (0.010 mmol Pt). Table includes reaction values for reference literature catalysts and catalyst **3**.

Figure 3b presents the hydrogenation of CO_2 to methane (Sabatier reaction) at low temperature (<150 ºC) catalyzed by the **2** and **3** and also by reference catalysts (further details including TOFs can be found in Table S3).[23] As it can be seen, catalyst **3** outperforms the rest of materials tested under the low–temperature conditions, including the industrial catalyst Ru–Al_2O_3. The lack of activity of **2** discards Pt^{2+} sites as catalytic active species, and indicates that Pt_2^0 is the catalytic sites for the

hydrogenation of CO_2 and that the Pt^{2+} sites are not *in–situ* reduced to Pt_2^0, in contrast to the cyanide reaction. It can be speculated that Pt^{2+} reduction occurs with CO, which is certainly prone to saturate the cation, in contrast to H_2, which should not have a significant interaction. The calculated energy of activation (E_a) for **3** (35 KJ mol^{-1}) is much lower than that of commercial catalysts ($E_a \approx 65$ KJ mol^{-1}), which opens the gate to perform the reaction at lower temperatures with Pt_2^0 catalytic sites.

In the present case, the dissociation of H_2 on Pt_2^0 may occur in two ways: 1) by metal–metal assisted hydrogen splitting, as it occurs in extended metal surfaces, to form an intermediate H–Pt–Pt–H species, or 2) by splitting in just one Pt atom, to give a Pt–Pt(H)H intermediate. While the former intermediate nicely explains the easy hydrogenation of CO_2 if hydrides attack to external CO_2, the latter intermediate should not be discarded since it can be formed prior to H–Pt–Pt–H species. Indeed, computational calculations have suggested that the splitting of H_2 onto an ideal Pt_2 species is energetically favored on one but not in two Pt atoms.[38] If so, Langmuir–Hinshelwood type mechanisms where both H_2 and a second reactant are concomitantly activated on Pt_2 in **3** would also be possible, provided the second reactant enters into the Pt–Pt(H)H intermediate. Figure 3c shows that **3** efficiently catalyzes the hydrogenation of ethylene under industrial reaction conditions, in flow, at just 60 ºC, and with a sustained TOF of 250 h^{-1} and a calculated energy of activation that compares positively to current industrial Pd catalysts ($E_a \approx 32$ KJ mol^{-1}).[39] Batch recycles showed the stability of **3** after reaction (4 cycles with further hydrogenation of ethylene). Other ≤C6 alkenes such as propylene, 1,3–butadiene, and 1-hexene, among others (Table S4), reacted similarly well, and when isomerically pure *E*-3-hexene was hydrogenated with **3** as a catalyst, the corresponding isomerized intermediate *Z*-3-hexene was found during reaction, which supports a Langmuir–Hinshelwood type mechanism. Thus, it can be said that Pt_2^0 catalyzes alkene hydrogenation at much lower temperature (60 ºC) than current industrial processes with nanoparticles (200–400 ºC).[39]

In summary, it has been possible to achieve the multi–gram scale chemical synthesis of 8 wt% sub–nanometer dinuclear clusters Pt^0_2 on a MOF. Multi–technique characterization, including X–ray crystallography, allowed unambiguously to determine the structure of the cluster.[40] The unusual Pt^0_2 species have a powerful catalytic behavior, allowing the synthesis of NH_4CN at room temperature, the hydrogenation of CO_2 at low temperature (<140 ºC) and the hydrogenation of alkenes at 60 ºC. Despite thermal limitations in the MOF avoid competition with thermally more robust metal solids at higher reaction temperatures, the intrinsic catalytic activity found for the supported and precisely-defined Pt_2 opens a new way for the design of much active catalysts, not only for the reactions shown here but also for other reactions where the methodology here presented could be applied.

Acknowledgements

This work was supported by the MINECO (Spain) (Projects CTQ2016–75671–P, CTQ2014-55178-R, MAT2013–40823–R and Excellence Units “Severo Ochoa” and “Maria de Maeztu” SEV–2012–0267 and MDM–2015–0538) and the Ministero dell’Istruzione, dell’Università e della Ricerca (Italy) and the Junta de Andalucía (FQM–195 and P11–FQM–7756). M. M. thanks the MINECO for a predoctoral contract. M. A. R.–C. thank MECD for a FPU scholarship Thanks are also extended to the Ramón y Cajal Program (E. P. and J.–C. H.–G.). M. L.–H. acknowledges the financial support from the Juan de la Cierva Fellowships Program of MINECO (IJCI–2014–19367). M. M and M. A. R.–C. have equally contributed to this work.

Keywords: metal-organic frameworks • structural flexibility • platinum • metal clusters • catalysis

[1] A. M. Argo, J. F. Odzak, F. S. Lai, B. C. Gates, *Nature* **2002**, *415*, 623–626.
[2] J. Oliver-Meseguer, J. R. Cabrero-Antonino, I. Dominguez, A. Leyva-Perez, A. Corma, *Science* **2012**, *338*, 1452–1455.
[3] A. Corma, P. Concepción, M. Boronat, M. J. Sabater, J. Navas, M. J. Yacaman, E. Larios, A. Posadas, M. A. López-Quintela, D. Buceta, et al., *Nat. Chem.* **2013**, *5*, 775–781.
[4] X. Kang, S. Wang, Y. Song, S. Jin, G. Sun, H. Yu, M. Zhu, *Angew. Chemie Int. Ed.* **2016**, *55*, 3611–3614.
[5] L. Liu, U. Díaz, R. Arenal, G. Agostini, P. Concepción, A. Corma, *Nat. Mater.* **2016**, *16*, 132–138.
[6] C. T. Campbell, *Science* **2002**, *298*, 811–814.
[7] M. Boronat, A. Leyva-Pérez, A. Corma, *Acc. Chem. Res.* **2014**, *47*, 834–844.
[8] Y. Lei, F. Mehmood, S. Lee, J. Greeley, B. Lee, S. Seifert, R. E. Winans, J. W. Elam, R. J. Meyer, P. C. Redfern, et al., *Science* **2010**, *328*, 224–228.
[9] S. Kitagawa, R. Matsuda, *Coord. Chem. Rev.* **2007**, *251*, 2490–2509.
[10] O. K. Farha, J. T. Hupp, *Acc. Chem. Res.* **2010**, *43*, 1166–1175.
[11] H. Furukawa, K. E. Cordova, M. O’Keeffe, O. M. Yaghi, *Science* **2013**, *341*, 974.
[12] F. R. Fortea-Pérez, M. Mon, J. Ferrando-Soria, M. Boronat, A. Leyva-Pérez, A. Corma, J. M. Herrera, D. Osadchii, J. Gascon, D. Armentano, et al., *Nat. Mater.* **2017**, *16*, 760–766.
[13] M. Mon, J. Ferrando-Soria, M. Verdaguer, C. Train, C. Paillard, B. Dkhil, C. Versace, R. Bruno, D. Armentano, E. Pardo, *J. Am. Chem. Soc.* **2017**, *139*, 8098–8101.
[14] Y. Inokuma, S. Yoshioka, J. Ariyoshi, T. Arai, Y. Hitora, K. Takada, S. Matsunaga, K. Rissanen, M. Fujita, *Nature* **2013**, *495*, 461–466.
[15] H. Liu, L. Chang, C. Bai, L. Chen, R. Luque, Y. Li, *Angew. Chemie Int. Ed.* **2016**, *55*, 5019–5023.
[16] M. Zhao, K. Yuan, Y. Wang, G. Li, J. Guo, L. Gu, W. Hu, H. Zhao, Z. Tang, *Nature* **2016**, *539*, 76–80.
[17] Q. Yang, Q. Xu, S.-H. Yu, H.-L. Jiang, *Angew. Chemie Int. Ed.* **2016**, *55*, 3685–3689.
[18] L. Liu, Y. Song, H. Chong, S. Yang, J. Xiang, S. Jin, X. Kang, J. Zhang, H. Yu, M. Zhu, *Nanoscale* **2016**, *8*, 1407–1412.
[19] X. Li, T. W. Goh, L. Li, C. Xiao, Z. Guo, X. C. Zeng, W. Huang, *ACS Catal.* **2016**, *6*, 3461–3468.
[20] J. Gascon, A. Corma, F. Kapteijn, F. X. Llabrés i Xamena, *ACS Catal.* **2014**, *4*, 361–378.
[21] J. Sauer, M. Bewersdorf, M. Köstner, M. Rinner, D. Wolf, in *Handb. Heterog. Catal.*, Wiley-VCH Verlag GmbH & Co. KGaA, Weinheim, Germany, **2008**.
[22] J. D. Holladay, K. P. Brooks, R. Wegeng, J. Hu, J. Sanders, S. Baird, *Catal. Today* **2007**, *120*, 35–44.
[23] K. Ghaib, K. Nitz, F.-Z. Ben-Fares, *ChemBioEng Rev.* **2016**, *3*, 266–275.
[24] J. Klankermayer, S. Wesselbaum, K. Beydoun, W. Leitner, *Angew. Chemie Int. Ed.* **2016**, *55*, 7296–7343.

[25] J. Gómez-Díaz, N. López, *J. Phys. Chem. C* **2011**, *115*, 5667–5674.
[26] M. Mon, F. Lloret, J. Ferrando-Soria, C. Martí-Gastaldo, D. Armentano, E. Pardo, *Angew. Chemie Int. Ed.* **2016**, *55*, 11167–11172.
[27] M. Mon, J. Ferrando-Soria, T. Grancha, F. R. Fortea-Pérez, J. Gascon, A. Leyva-Pérez, D. Armentano, E. Pardo, *J. Am. Chem. Soc.* **2016**, *138*, 7864–7867.
[28] M. S. Rosen, A. M. Spokoyny, C. W. Machan, C. Stern, A. Sarjeant, C. A. Mirkin, *Inorg. Chem.* **2011**, *50*, 1411–1419.
[29] J. Tauchman, I. Císařová, P. Štěpnička, *Dalt. Trans.* **2014**, *43*, 1599–1608.
[30] P. S. Hall, D. A. Thornton, G. A. Foulds, *Polyhedron* **1987**, *6*, 85–94.
[31] M. Mihaylov, K. Chakarova, K. Hadjiivanov, O. Marie, M. Daturi, *Langmuir* **2005**, *21*, 11821–11828.
[32] S.-I. Tanaka, J. Miyazaki, D. K. Tiwari, T. Jin, Y. Inouye, *Angew. Chemie Int. Ed.* **2011**, *50*, 431–435.
[33] E. Pierce, E. Lanthier, C. Genre, Y. Chumakov, D. Luneau, C. Reber, *Inorg. Chem.* **2010**, *49*, 4901–4908.
[34] A. FERNANDEZ, I. LEZCANOGONZALEZ, M. BORONAT, T. BLASCO, A. CORMA, *J. Catal.* **2007**, *249*, 116–119.
[35] M. P. Elsner, C. Dittrich, D. W. Agar, *Chem. Eng. Sci.* **2002**, *57*, 1607–1619.
[36] D. Britt, D. Tranchemontagne, O. M. Yaghi, *Proc. Natl. Acad. Sci.* **2008**, *105*, 11623–11627.
[37] T. G. Appleton, J. R. Hall, S. F. Ralph, *Inorg. Chem.* **1985**, *24*, 4685–4693.
[38] Q. Cui, D. G. Musaev, K. Morokuma, *J. Chem. Phys.* **1998**, *108*, 8418–8428.
[39] H. Zea, K. Lester, A. K. Datye, E. Rightor, R. Gulotty, W. Waterman, M. Smith, *Appl. Catal. A Gen.* **2005**, *282*, 237–245.
[40] L. Liu, D. N. Zakharov, R. Arenal, P. Concepcion, E. A. Stach, A. Corma, *Nat. Commun.* **2018**, *9*, 574.